npj | quantum materials

Article

Published in partnership with Nanjing University

https://doi.org/10.1038/s41535-024-00688-6

Charge order near the antiferromagnetic quantum critical point in the trilayer high T_c cuprate $HgBa_2Ca_2Cu_3O_{8+\delta}$

V. Oliviero[1,5], I. Gilmutdinov[1,5], D. Vignolles[1], S. Benhabib[1,4], N. Bruyant[1], A. Forget[2], D. Colson[2], W. A. Atkinson[3] ✉ & C. Proust[1] ✉

We study the transport properties of underdoped trilayer cuprate $HgBa_2Ca_2Cu_3O_{8+\delta}$ with doping level $p = 0.10$–0.12 in magnetic field up to 88 T. We report for the first time in a cuprate superconductor a dramatic change of the quantum oscillation spectrum versus temperature, which is accompanied by a sign change of the Hall effect below $T \approx 10$ K. Based on numerical simulations, we infer a Fermi surface reconstruction in the inner plane from an antiferromagnetic state (hole pockets) to a biaxial charge density wave state (electron pockets). We show that both orders compete and share the same hotspots of the Fermi surface, and we discuss our result in the context of spin-fermion models.

One of the surprising features of cuprate superconductors is the ubiquity of the interplay between antiferromagnetic (AFM) order, charge density waves (CDWs), and superconductivity[1]. In general, these orders compete, and each occupies its own piece of the phase diagram; however, significant coexistence regimes are observed, and these can lead to novel cooperative behavior. For example, incommensurate CDW and spin orders coexist as magnetic stripes in the La-based cuprates[2,3]. In other cuprates, CDWs are nonmagnetic, and there have been ongoing efforts to understand their connection to the strong electron correlations, low dimensionality, and AFM fluctuations that are hallmarks of the cuprates[1]. The Peierls paradigm that requires extended sections of Fermi surface to be nested by some wavevector $\mathbf{q}$, leading to a peak in the non-interacting charge susceptibility, is certainly not at the origin of the cuprate CDWs. There are other CDW materials without obvious Fermi surface nesting—for example, layered dichalcogenides such as $NbSe_2$[4] and nonmagnetic pnictides in the $BaNi_2As_2$ family[5]—for which there is compelling evidence that the CDWs are phonon-driven[6–9]. The corresponding evidence in the cuprates is weak[10].

As an alternative to phonons, spin fluctuations provide a natural mechanism for CDW formation in cuprates. The mechanism for cuprate superconductivity is widely accepted to be of magnetic origin[11], and several analytical calculations predict that spin-fluctuation-mediated CDWs degenerate with superconductivity at the AFM quantum critical point (where the Néel temperature vanishes)[12–15]. This is important because it provides a route to charge order at high temperatures without Fermi surface nesting. Instead, CDW wavevectors connect Fermi surface "hotspots" that are determined by the $\mathbf{q}$-dependence of the spin susceptibility. Early versions of the theory incorrectly predicted that the CDW $\mathbf{q}$-vectors lie along the Brillouin zone diagonals, with $\mathbf{q} = (q, \pm q)$; however, quantitatively correct axial CDW wavevectors, $\mathbf{q} = (q, 0), (0, q)$, are obtained when the dominant diagonal-$\mathbf{q}$ instability is suppressed. This occurs close to the AFM quantum critical point[16–18], within AFM[19,20] or loop-current[21] phases, or when strong correlations are accounted for (see refs. 22–25). Note, however, that realistic band structures produce weak peaks in the bare charge susceptibility with similar $\mathbf{q}$-vectors[26] despite the lack of proper Fermi surface nesting. Thus, while there is experimental support for Fermi surface hotspots[27], it is unresolved whether they are selected by the Fermi surface or the interaction.

CDWs have clear signatures in the transport properties of $YBa_2Cu_3O_{6+x}$ (YBCO) and single-layer $HgBa_2CuO_{4+\delta}$ (Hg1201). At low temperatures, the observation of small-frequency quantum oscillations[28,29] combined with negative Hall[30–32] and Seebeck[32–34] coefficients indicate the presence of a closed electron pocket in the reconstructed Fermi surface. Details of the reconstruction are still debated[35], but a plausible scenario is a biaxial charge order that creates a small electron-like pocket located at the nodes. Quantum oscillations with small frequencies have also been observed in the underdoped trilayer cuprate $HgBa_2Ca_2Cu_3O_{8+\delta}$ (Hg1223) at hole doping $p = 0.08$–0.09 but without a sign change in the Hall coefficient down to the lowest temperatures[36]. A plausible interpretation is the coexistence of an AFM order in the inner plane and CDW in the outer planes. Multilayer cuprates, with three or more CuO_2 layers per unit cell, offer a new twist on the story because a single material can host distinct phases in different layers simultaneously[37]. This raises intriguing questions about the coexistence and

[1]LNCMI-EMFL, CNRS UPR3228, Univ. Grenoble Alpes, Univ. Toulouse, INSA-T, Grenoble and Toulouse, Toulouse, France. [2]Service de Physique de l'Etat Condensé, CEA Saclay (CNRS-URA 2464), Gif sur Yvette, 91191, France. [3]Department of Physics and Astronomy, Trent University, Peterborough, K9L 0G2 ON, Canada. [4]Present address: Laboratoire de Physique des Solides, 91405 Orsay, France. [5]These authors contributed equally: V. Oliviero, I. Gilmutdinov.
✉e-mail: billatkinson@trentu.ca; cyril.proust@lncmi.cnrs.fr

competition between these phases, and the possible emergence of novel cooperative phases. In particular, symmetry-inequivalent CuO_2 planes differ both in doping and disorder levels[37–40]. In addition, AFM order is more robust in multilayer cuprates and persists up to higher doping as the number of CuO_2 planes increases[37].

Results

Hall effect measurements

Figure 1a shows the Hall coefficient plotted as a function of magnetic field H for Hg1223 $p = 0.118$ at different temperatures from $T = 20$ K down to $T = 4.2$ K. While R_H is positive above $T = 20$ K, it becomes negative at $T = 4.2$ K and flattens at fields above $H \approx 70$ T, which indicates that the normal state is reached. The temperature-dependence of the normal-state Hall coefficient measured at the highest fields (see Supplementary Note 5) between $T = 1.5$ K and 100 K is shown in Fig. 1b at three doping levels, $p = 0.118$ and $p = 0.101$ (this work) and $p = 0.089$[36]. For $p = 0.118$ and $p = 0.101$, there is a sudden sign change of the Hall coefficient below $T \approx 10$ K that is not observed at lower doping. The sign change is accompanied by a maximum of the resistance at $T \approx 10$ K (see Fig. 1c for $p = 0.118$). In other cuprates, notably underdoped YBCO[41–43] and Hg1201[44,45], this behavior is attributed to the emergence of charge order. Here, both the abruptness of the transition and its low temperature, are surprising.

Quantum oscillation measurements

Because of the low temperatures, we are in the rare situation of being able to track the Fermi surface morphology through the CDW transition using quantum oscillation measurements. Figure 2a shows the variation of the tunnel diode oscillator (TDO) circuit frequency as a function of the magnetic field at different temperatures for the $p = 0.112$ sample (see Methods). A smooth background subtraction leads to the oscillatory part of the signal depicted in Fig. 2b. At $T = 4.2$ K, there is a strong low-frequency oscillation whose amplitude decreases with decreasing temperature. By $T = 1.75$ K, the low-frequency oscillations are weak, and small amplitude oscillations at higher frequencies have emerged. This is inconsistent with the Lifshitz–Kosevich theory for a temperature-independent Fermi surface[46], but rather signals a Fermi surface reconstruction. The temperature evolution of the oscillation spectrum is clearly seen in the Fourier analysis of the oscillatory part of the data (Fig. 2c). At $T = 4.2$ K, the spectrum is dominated by a low-frequency peak ($F = 680$ T, black arrow) and its first harmonic. The low-frequency peak weakens and shifts to a higher frequency ($F = 830$ T) as the temperature decreases. Two peaks at high frequency, $F = 2100$ T and $F = 2800$ T (red arrow), emerge at the lowest temperatures. While the high frequencies could result from a large effective mass (a Lifshitz–Kosevich analysis for $F = 2800$ T would have given $m^* = 6.3 \pm 0.5\, m_e$, see Supplementary Fig. 6), the Fermi surface reconstruction scenario is required by the T-dependence of the low-frequency oscillation. Note that the evolution of the quantum oscillation spectrum versus temperature has been reproduced in another sample at doping level $p = 0.102$ (see Supplementary Fig. 7 and Notes 6). The comparison of quantum oscillations in Hg1223 at different doping levels from $p = 0.080$ to $p = 0.112$ is shown in Supplementary Fig. 8.

Theory

Our results demonstrate that a crossover takes place at low temperatures for $p = 0.10$–0.12 when superconductivity is quenched by a magnetic field. To gain insight, we numerically simulated quantum oscillations of the density of states for a single CuO_2 trilayer. Since the detailed band structure of underdoped Hg1223 is unknown, the trilayer model was adapted from existing tight-binding models for related multilayer compounds (see Supplementary Note 1). A layer-dependent quasiparticle scattering rate, which modifies QO amplitudes but not frequencies, was incorporated. We then introduced, by hand, commensurate AFM and CDW order parameters. The AFM and CDW magnitudes, and the CDW periodicity, are the main tuning parameters in our model, and they were adjusted to give plausible oscillation spectra at each temperature.

We found that CDW order alone is insufficient, but that the addition of AFM order in the inner layer explains the measured oscillations. The required AFM order parameter, $M \lesssim 50$ meV, is small compared to the values $M \gtrsim 100$ meV inferred from experiments at slightly smaller doping[36,39]. Consistent with this substantial change of energy scales, NMR experiments on related multilayer cuprates[37] find that the Néel temperature collapses rapidly near the end of the metallic AFM phase. Taken together, these suggest that the current doping is close to the AFM quantum critical point. We introduce CDW order parameters Δ_i and Δ_o for the inner and outer layers, respectively. The CDWs are biaxial, with wavevectors of magnitude $q = 2\pi/4.5a_0$, and with a bond-centered d-wave form factor. The true form factor is more complex[47], but would not change our results qualitatively. Similarly, the calculated QOs are not strongly dependent on the value of Δ_o, which we cannot therefore establish reliably. Conversely, our results are highly sensitive to both q and Δ_i. We include scattering rates $\Gamma_{o,\mathbf{k}}$ and $\Gamma_{i,\mathbf{k}}$ for the outer and inner layers, respectively. We assume that $\Gamma_{o,\mathbf{k}}$ is impurity-dominated, and, therefore, isotropic and T-independent, while $\Gamma_{i,\mathbf{k}}$ is anisotropic—either due to pseudogap physics or to order parameter fluctuations—and decreases with decreasing T.

The density of states, $N_0(H)$, is obtained at the Fermi energy as a function of magnetic field using a numerical recursion method for large supercells (see Supplementary Note 2), for the parameters in Table 1. Figure

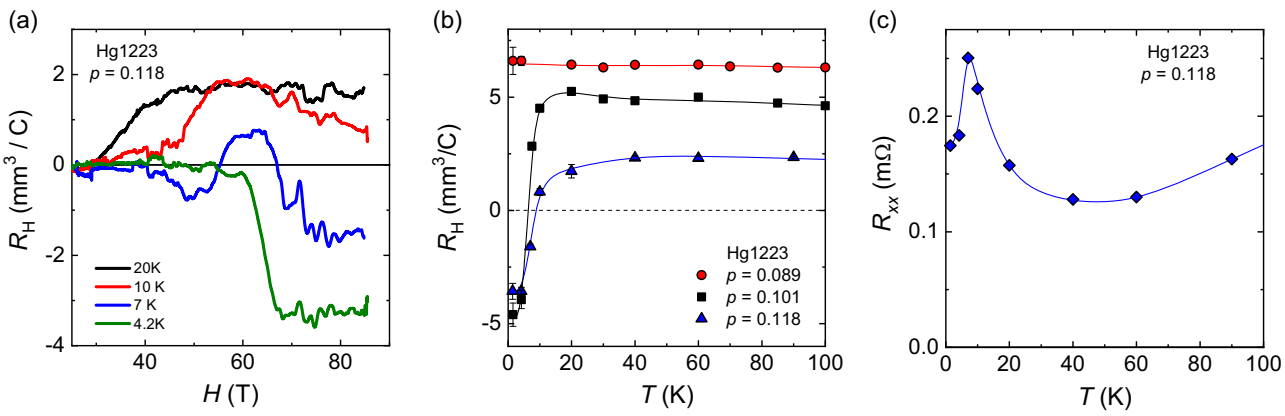

Fig. 1 | Transport measurements in Hg1223. a Field dependence of the Hall coefficient R_H in Hg1223 ($p = 0.118$) at various fixed temperatures, as indicated. **b** Temperature dependence of the normal-state Hall coefficient R_H, measured at high fields (see Supplementary Note 5), in Hg1223 $p = 0.089$ (red circles from ref. 36), $p = 0.101$ (black squares, this work), and $p = 0.118$ (blue triangles, this work). At $p = 0.101$ and $p = 0.118$, R_H changes sign abruptly below $T = 10$ K while it remains positive down to the lowest temperature for $p = 0.089$. **c** Temperature dependence of the normal-state resistance in Hg1223 ($p = 0.118$). The sign change of the Hall coefficient is accompanied by a maximum in the resistance, that strongly suggests the occurrence of a phase transition.

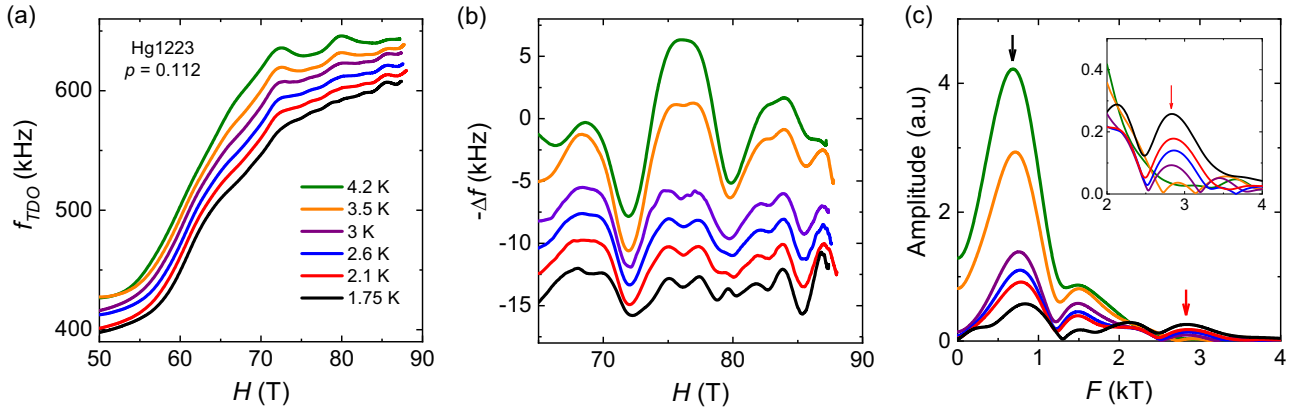

Fig. 2 | Quantum oscillation measurements in Hg1223. a Field dependence of the TDO frequency after the heterodyne circuit in Hg1223 ($p = 0.112$) at various fixed temperatures, as indicated. **b** Oscillatory part of the TDO signal after removing a smooth background (spline) from the data shown in panel (**a**). $-\Delta f$ is plotted and the curves have been offset for clarity. At $T = 4.2$ K, only two oscillations are detected due to the small field window above the superconducting transition. Their amplitude does not increase significantly with the magnetic field, which is likely due to the presence of closely spaced frequencies and a beating-like effect. **c** Discrete Fourier analysis of the oscillatory part of the TDO signal shown in panel (**b**) in the field range 70 T $\leq H \leq$ 87 T. The black (red) arrow marks the low (high) frequency observed at $T = 4.2$ K ($T = 1.8$ K). The broadening of the Fourier transform at low frequency comes from the small number of oscillations in the field range. The inset shows a zoom of the Fourier transform between $F = 2$ kT and $F = 4$ kT, where one can clearly see the emergence of two peaks at $F = 2100$ T and $F = 2800$ T (red arrow).

Table 1 | *T*-dependent order parameters and scattering rates used to simulate quantum oscillations at $T = 4.2$ K and $T = 1.8$ K

	$T = 4.2$ K	$T = 1.8$ K
M	0.3	0.05
Δ_o	0.1	0.15
Δ_i	0.0	0.1
$\Gamma_{o,\mathbf{k}}$	0.020	0.020
$\Gamma_{i,\mathbf{k}}$	$0.005 + 0.005\eta_{\mathbf{k}}^2$	$0.005 + 0.002\eta_{\mathbf{k}}^2$

Values are in units of the outer-layer nearest-neighbor hopping matrix element, t_{o1} ~170 meV and $\eta_{\mathbf{k}} = \cos k_x - \cos k_y$. Tight-binding band parameters (given in Supplementary Notes 1) are held constant.

3a shows that the oscillations at 4.2 K are dominated by a single frequency, while multiple frequencies are evident at 1.8 K. Fourier transforming with respect to $1/H$ reveals a strong low-frequency peak at $F \approx 600$ T at 4.2 K, along with harmonics at 1200 and 1800 T [Fig. 3b]. The peak weakens and shifts to a higher frequency, $F \approx 800$ T, at 1.8 K. Additional peaks, most notably at 1100 and 2700 T, emerge at low T. These frequencies agree surprisingly well with the experiments.

The reconstructed Fermi surfaces are too complicated to provide a semiclassical explanation of the peaks (see Fig. 1 of the Supplementary Information). Simplified Fermi surfaces [Fig. 3c, d)] show that the main peak at 4.2 K comes from hole pockets (blue) generated by AFM order; the other Fermi surfaces (solid red and green) are unchanged by AFM because they have primarily outer-layer character, but are reconstructed by the outer-layer CDW to form electron pockets (dashed red and green). By assumption, the inner-layer order parameters M and Δ_i depend on T. Consequently, the main peak's frequency increases between 4.2 K and 1.8 K because the hole pocket area grows as M decreases; the peak's height decreases because of increased quasiparticle scattering by the CDW (Δ_i grows as T decreases) and magnetic breakdown when M is small. Ultimately, Δ_i reconstructs the hole pocket at low T to form a diamond-shaped electron pocket [dashed blue in Fig. 3d] with frequency, F ~2700 T. This provides an explanation for the high-frequency peak seen experimentally [Fig. 2c]. Other low-T peaks in Fig. 3b, at 1100 and 2100 T, are clearly tied to the growth of Δ_i, but are difficult to ascribe to a single semiclassical orbit.

Discussion

Our calculations support the scenario shown in Fig. 4. Above 10 K, inner-layer AFM order coexists with short-range outer-layer CDW order. Below 10 K, the CDW is sufficiently long-range that the outer-layer Fermi surfaces are reconstructed and generate an electron-like Hall coefficient; however, the relatively large quasiparticle scattering rate in the outer layers damps the corresponding quantum oscillations. (In our simulations, the outer layers account for less than 10% of oscillation amplitude.) Though centered on different layers, the AFM and CDW orders compete because the layers are coupled, and the CDW order gradually replaces the AFM order on the inner layer. In our simulations, the shifts of the main peak height and frequency, and the appearance of a high-frequency peak are intimately connected to this crossover. While zero-field charge order was detected in Hg1223[48], we cannot exclude that it is enhanced by the magnetic field, as in YBCO[49].

The results reported here have a remarkable implication. In our simulations, the CDW wavevector q was chosen to explain the low-T oscillation peak at ~2800 T. The CDW hotspots implied by this q-value are, within the resolution of our simulations, coincident with the AFM hotspots, i.e., points on the Fermi surface connected by the AFM wavevector $\mathbf{Q} = (\frac{\pi}{a_0}, \frac{\pi}{a_0})$ (Fig. 4 bottom). This coincidence is a key feature of models in which CDW order is mediated by critical spin fluctuations carrying momentum $\mathbf{Q}$. In contrast, the CDW order tends to connect points away from the AFM hotspots when it emerges on top of a pre-existing AFM state[20,50]. As discussed above, we infer from our measurements that the AFM quantum critical point is nearby. Our measurements are thus suggestive that charge order at this doping level is mediated by critical spin fluctuations.

One possible counter-argument is that the superconducting and long-range CDW transition temperatures differ by an order of magnitude, contrary to early calculations suggesting they should be the same at the AFM quantum critical point[13,14]; however, more recent work showed that the predicted degeneracy breaks down when the band structure lacks particle-hole symmetry[19], as in Hg1223. Another possible counter-argument is that CDW order persists in YBCO[51], in $La_{2-x}Sr_xCuO_4$[52], and in overdoped $Tl_2Ba_2CuO_{6+\delta}$[53] to doping levels far from the AFM quantum critical point. It is unlikely that the AFM hotspot picture makes sense in these doping regimes, and other (noncritical) interactions are likely important. The question posed by our work is whether the hotspot picture makes sense close to the AFM quantum critical point. In this regard, it would be interesting to determine the evolution of the CDW wavevectors with doping because the CDW hotspots should be pinned to the AFM Brillouin zone boundary wherever critical spin fluctuations are the dominant interaction.

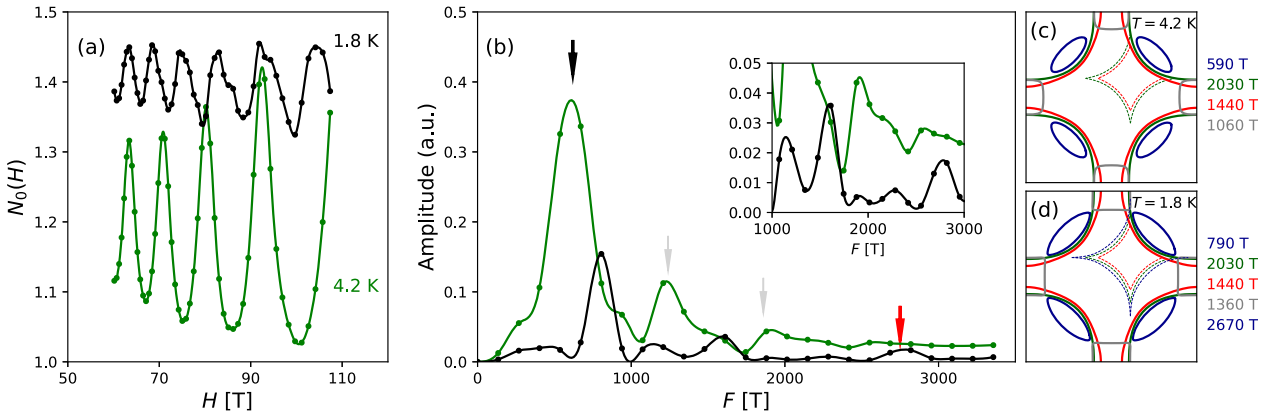

Fig. 3 | Simulation of the density of states in Hg1223. a Calculated density of states $N_0(H)$ at the Fermi energy as a function of magnetic field H for $T = 4.2$ K and $T = 1.8$ K and **b** its Fourier transform, using the parameters in Table 1. The inset shows an expanded view of the high-frequency region. Arrows indicate the low- (black) and high-frequency (red) peaks and their harmonics (gray). **c**, **d** Show simplified Fermi surfaces for the 4.2 and 1.8 K, respectively. Quantum oscillation frequencies calculated from the Fermi surface areas are listed next to each panel.

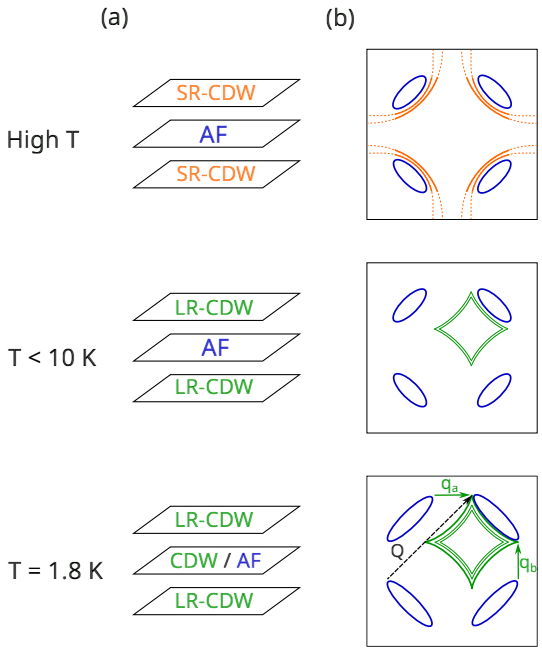

Fig. 4 | Sketch of the Fermi surface. a Sketch of the trilayer structure of Hg1223 in different temperature ranges. SR(LR)-CDW stands for short-range (long-range) CDW and AF corresponds to antiferromagnetism. **b** Sketch of the Fermi surface corresponding to the sequence of crossover as the temperature is reduced (see text). $\mathbf{q}_a = (q, 0)$ and $\mathbf{q}_b = (0, q)$ are the wavevector of the biaxial CDW. **Q** is the AFM wavevector.

The fact that the CDW and AFM Fermi surface hotspots coincide in our simulations provides a natural explanation for the competition between the two phases: both phases derive part of their condensation energy from the gap they open at the hotspot and the phase with the largest condensation energy will form preferentially. Our model suggests that these energies must be roughly equal at 4.2 K, and that there is growth of the outer-layer CDW below 4.2 K that tips the balance in the inner layer toward the CDW phase. Since the order parameters reported in Table 1 are directly related to the hotspot gaps, it is tempting to make naive statements about the energetics of the competition between the CDW and AFM phases. Noting that the d-wave character of the CDW means that the CDW gap near the antinode is roughly twice the value shown in the table, and that Δ_o is not well-established by our simulations and could be significantly larger, it is plausible that the AFM and CDW phases have similar gap magnitudes. However, these arguments miss the important point that the CDW and AFM condensation energies have distinct dependencies on the Fermi surface geometry (unlike BCS superconductors, which depend only on the density of states). Simple arguments about the energetics of the two phases are, therefore, not possible, and a proper microscopic calculation is required.

In conclusion, we have measured the evolution of the Fermi surface at low temperatures in Hg1223 samples with $p = 0.10$–0.12, and demonstrated that there is a Fermi surface reconstruction at low temperature. Through numerical simulations, we attribute this to competition between CDW and AFM order. The CDW wavevectors required to reproduce the experimental oscillation spectrum suggest that the CDW and AFM phases share Fermi surface hotspots. This naturally explains the competition between the two phases, but is also a hallmark of CDWs that are mediated by critical spin fluctuations.

Table 2 | T_c, hole doping and probe measurement for the five Hg1223 samples measured in this study

sample	T_c	p	measurements
Hg1223	114 K	0.118	transport
Hg1223	108 K	0.112	TDO
Hg1223	95 K	0.101	transport
Hg1223	96 K	0.102	TDO
Hg1223	78 K	0.089	transport[36]

Methods

Samples

Single crystals of the trilayer cuprate $HgBa_2Ca_2Cu_3O_{8+\delta}$ have been synthesized using a self-flux growth technique as described in ref. 54. Using adequate heat treatment, Hg1223 can be largely underdoped and its doping level controlled. The doping p has been deduced from the empirical relation $1 - T_c/T_{c,\max} = 82.6(p-0.16)^2$, where T_c is the onset superconducting transition measured by SQUID (see Supplementary Fig. 3) and $T_{c,\max} = 133$ K. The list of samples studied by transport or TDO are shown in Table 2 with their T_c and corresponding hole doping. The results for the lowest doping $p = 0.089$ are from ref. 36.

TDO measurements

Quantum oscillation measurements using the tunnel diode oscillator technique[55,56] were performed at the pulsed-field facility in Toulouse

(LNCMI-T) up to 88 T in two samples of Hg1223 at doping levels $p = 0.102$ ($T_c = 96$ K) and $p = 0.112$ ($T_c = 108$ K). Typical sample dimensions are $500 \times 500 \times 100$ μm^3. The experimental setup consists of an LC-tank circuit powered by a tunneling diode oscillator biased in the negative resistance region of the current-voltage characteristic. The sample is placed in a compensated 8-shape coil (the diameter and length of the coil are adapted for each sample to optimize the filling factor). The fundamental resonant frequency f_0 of the whole circuit is about 25 MHz. The RF signal is amplified and demodulated down to a frequency of about 1 MHz using a heterodyne circuit. A high-speed acquisition system is used to digitize the signal. The data are post-analysed using a software to extract the field dependence of the resonance frequency f_{TDO}, which is sensitive to the resistivity through the change in skin depth.

Hall effect measurements

The Hall effect was measured at the LNCMI-T in two distinct samples of Hg1223 at similar doping levels, $p = 0.101$ ($T_c = 95$ K) and $p = 0.118$ ($T_c = 114$ K). The magnetic field H was applied along the c-axis of the tetragonal structure, perpendicular to the CuO_2 planes for both field polarities. Data for the sample $p = 0.089$ is from ref. 36. Typical sample dimensions are $700 \times 400 \times 90$ μm^3. Gold contacts were sputtered onto the surface of the sample before a heat treatment leading to contact resistances of a few ohms at room temperature and below 1 Ω at low temperature. The measurements were performed up to 86 T in a dual coil magnet using a conventional four-point configuration with a current excitation of ≈5 mA at a frequency of ≈60 kHz. A high-speed acquisition system was used to digitize the reference signal (current) and the voltage drop across the sample at a frequency of 500 kHz. The data were post-analyzed with software to perform the phase comparison.

Calculations

We numerically simulated quantum oscillations of the density of states for a tight-binding model of a single CuO_2 trilayer using a numerical recursion method for large supercells (see Supplementary Notes 1, 2 for a detailed description).

Data availability

The data that support the findings of this study are available from the corresponding authors upon reasonable request.

Code availability

The codes used during the current study are available from the corresponding author on reasonable request.

Received: 20 June 2024; Accepted: 22 September 2024;
Published online: 04 October 2024

References

1. Keimer, B., Kivelson, S., Norman, M., Uchida, S. & Zaanen, J. From quantum matter to high-temperature superconductivity in copper oxides. *Nature* **518**, 179–186 (2015).
2. Frano, A., Blanco-Canosa, S., Keimer, B. & Birgeneau, R. J. Charge ordering in superconducting copper oxides. *J. Phys. Condens. Matter* **32**, 374005 (2020).
3. Uchida, S. Ubiquitous charge order correlations in high-temperature superconducting cuprates. *J. Phys. Soc. Jpn.* **90**, 111001 (2021).
4. Zhu, X., Guo, J., Zhang, J. & Plummer, E. W. Misconceptions associated with the origin of charge density waves. *Adv. Phys. X* **2**, 622–640 (2017).
5. Lee, S. et al. Unconventional charge density wave order in the pnictide superconductor $Ba(Ni_{1-x}Co_x)_2As_2$. *Phys. Rev. Lett.* **122**, 147601 (2019).
6. Johannes, M. D. & Mazin, I. I. Fermi surface nesting and the origin of charge density waves in metals. *Phys. Rev. B* **77**, 433 (2008).
7. Weber, F. et al. Optical phonons and the soft mode in 2H-$NbSe_2$. *Phys. Rev. B* **87**, 245111 (2013).
8. Souliou, S. et al. Soft-phonon and charge-density-wave formation in nematic $BaNi_2As_2$. *Phys. Rev. Lett.* **129**, 247602 (2022).
9. Song, Y. et al. Phonon softening and slowing-down of charge density wave fluctuations in $BaNi_2As_2$. *Phys. Rev. B* **107**, L041113 (2023).
10. Souliou, S.-M. et al. In-plane isotropy of the low energy phonon anomalies in $YBaCu_3O_{6+x}$. *J. Phys. Soc. Jpn.* **90**, 111006 (2021).
11. Scalapino, D. J. A common thread: the pairing interaction for unconventional superconductors. *Rev. Mod. Phys.* **84**, 1383–1417 (2012).
12. Metlitski, M. & Sachdev, S. Quantum phase transitions of metals in two spatial dimensions. II. Spin density wave order. *Phys. Rev. B* **82**, 075128 (2010).
13. Metlitski, M. & Sachdev, S. Instabilities near the onset of spin density wave order in metals. *New J Phys.* **12**, 105007 (2010).
14. Efetov, K. B., Meier, H. & Pépin, C. Pseudogap state near a quantum critical point. *Nat. Phys.* **9**, 442–446 (2013).
15. Wang, Y. & Chubukov, A. Charge-density-wave order with momentum (2q, 0) and (0, 2q) within the spin-fermion model: continuous and discrete symmetry breaking, preemptive composite order, and relation to pseudogap in hole-doped cuprates. *Phys. Rev. B* **90**, 035149 (2014).
16. Pépin, C., Carvalho, V. S. D., Kloss, T. & Montiel, X. Pseudogap, charge order, and pairing density wave at the hot spots in cuprate superconductors. *Phys. Rev. B* **90**, 195207 (2014).
17. Allais, A., Bauer, J. & Sachdev, S. Density wave instabilities in a correlated two-dimensional metal. *Phys. Rev. B* **90**, 155114 (2014).
18. Tsuchiizu, M., Yamakawa, Y. & Kontani, H. p-Orbital density wave with d symmetry in high-T_c cuprate superconductors. *Phys. Rev. B* **93**, 155148 (2016).
19. Wang, X., Wang, Y., Schattner, Y., Berg, E. & Fernandes, R. M. Fragility of charge order near an antiferromagnetic quantum critical point. *Phys. Rev. Lett.* **120**, 247002 (2018).
20. Atkinson, W. A., Kampf, A. P. & Bulut, S. Charge order in the pseudogap phase of cuprate superconductors. *N. J. Phys.* **17**, 013025 (2015).
21. Atkinson, W. A., Kampf, A. P. & Bulut, S. Emergence of charge order in a staggered loop-current phase of cuprate high-temperature superconductors. *Phys. Rev. B* **93**, 134517 (2016).
22. Chowdhury, D. & Sachdev, S. Density-wave instabilities of fractionalized fermi liquids. *Phys. Rev. B* **90**, 245136 (2014).
23. Banerjee, S., Atkinson, W. & Kampf, A. P. Emergent charge order from correlated electron-phonon physics in cuprates. *Commun. Phys.* **3**, 161 (2020).
24. Banerjee, A., Pépin, C. & Ghosal, A. Charge, bond, and pair density wave orders in a strongly correlated system. *Phys. Rev. B* **105**, 134505 (2022).
25. Mascot, E. et al. Electronic spectra with paramagnon fractionalization in the single-band Hubbard model. *Phys. Rev. B* **105**, 075146 (2022).
26. Sachdev, S. & La Placa, R. Bond order in two-dimensional metals with antiferromagnetic exchange interactions. *Phys. Rev. Lett.* **111**, 027202 (2013).
27. Atkinson, W. A., Ufkes, S. & Kampf, A. P. Structure of the charge density wave in cuprate superconductors: lessons from NMR. *Phys. Rev. B* **97**, 125147 (2018).
28. Doiron-Leyraud, N. et al. Quantum oscillations and the fermi surface in an underdoped high-t c superconductor. *Nature* **447**, 565–568 (2007).
29. Barišić, N. et al. Universal quantum oscillations in the underdoped cuprate superconductors. *Nat. Phys.* **9**, 761–764 (2013).
30. LeBoeuf, D. et al. Electron pockets in the fermi surface of hole-doped high-T_c superconductors. *Nature* **450**, 533–536 (2007).
31. LeBoeuf, D. et al. Lifshitz critical point in the cuprate superconductor $YBa_2Cu_3O_y$ from high-field hall effect measurements. *Phys. Rev. B* **83**, 054506 (2011).
32. Doiron-Leyraud, N. et al. Hall, Seebeck, and nernst coefficients of underdoped $HgBa_2CuO_{4+\delta}$: Fermi-surface reconstruction in an archetypal cuprate superconductor. *Phys. Rev. X* **3**, 021019 (2013).

33. Chang, J. et al. Nernst and seebeck coefficients of the cuprate superconductor $YBa_2Cu_3O_{6.67}$: a study of fermi surface reconstruction. *Phys. Rev. Lett.* **104**, 057005 (2010).
34. Laliberté, F. et al. Fermi-surface reconstruction by stripe order in cuprate superconductors. *Nat. Commun.* **2**, 432 (2011).
35. Proust, C. & Taillefer, L. The remarkable underlying ground states of cuprate superconductors. *Ann. Rev. Cond. Matt. Phys.* **10**, 409–429 (2019).
36. Oliviero, V. et al. Magnetotransport signatures of antiferromagnetism coexisting with charge order in the trilayer cuprate $HgBa_2Ca_2Cu_3O_{8+\delta}$. *Nat. Commun.* **13**, 1568 (2022).
37. Mukuda, H., Shimizu, S., Iyo, A. & Kitaoka, Y. High-T_c superconductivity and antiferromagnetism in multilayered copper oxides: a new paradigm of superconducting mechanism. *J. Phys. Soc. Jpn.* **81**, 011008 (2012).
38. Ideta, S. et al. Enhanced superconducting gaps in the trilayer high-temperature $Bi_2Sr_2Ca_2Cu_3O_{10+\delta}$ cuprate superconductor. *Phys. Rev. Lett.* **104**, 227001 (2010).
39. Kunisada, S. et al. Observation of small fermi pockets protected by clean CuO_2 sheets of a high-T_c superconductor. *Science* **369**, 833–838 (2020).
40. Luo, X. et al. Electronic origin of high-T_c maximization and persistence in trilayer cuprate superconductors. *Nature Phys.* **13**, 1841–1847 (2023).
41. Wu, T. et al. Magnetic-field-induced charge-stripe order in the high-temperature superconductor $YBa_2Cu_3O_y$. *Nature* **477**, 191–194 (2011).
42. Ghiringhelli, G. et al. Long-range incommensurate charge fluctuations in $(Y,Nd)Ba_2Cu_3O_{6+x}$. *Science* **337**, 821–825 (2012).
43. Chang, J. et al. Direct observation of competition between superconductivity and charge density wave order in $YBa_2Cu_3O_{6.67}$. *Nat. Phys.* **8**, 871–876 (2012).
44. Tabis, W. et al. Charge order and its connection with fermi-liquid charge transport in a pristine high-T_c cuprate. *Nat. Commun.* **5**, 5875–5880 (2014).
45. Chan, M. K. et al. Extent of fermi-surface reconstruction in the high-temperature superconductor $HgBa_2CuO_{4+\delta}$. *Proc. Natl Acad. Sci. USA* **117**, 9782–9786 (2020).
46. Shoenberg, D. *Magnetic Oscillations in Metals* (Cambridge Univ. Press, 1984).
47. McMahon, C. et al. Orbital symmetries of charge density wave order in $YBa_2Cu_3O_{6+x}$. *Sci. Adv.* **6**, eaay0345 (2020).
48. Loret, B. et al. Intimate link between charge density wave, pseudogap and superconducting energy scales in cuprates. *Nat. Phys.* **15**, 771–775 (2019).
49. Gerber, S. et al. Three-dimensional charge density wave order in $YBa_2Cu_3O_{6.67}$ at high magnetic fields. *Science* **350**, 949–952 (2015).
50. Harrison, N. Robustness of the biaxial charge density wave reconstructed electron pocket against short-range spatial antiferromagnetic fluctuations. *Phys. Rev. B* **97**, 245150 (2018).
51. Blanco-Canosa, S. et al. Resonant x-ray scattering study of charge-density wave correlations in $YBa_2Cu_3O_{6+x}$. *Phys. Rev. B* **90**, 054513 (2014).
52. Wen, J.-J. et al. Observation of two types of charge-density-wave orders in superconducting $La_{2-x}Sr_xCuO_4$. *Nat. Commun.* **10**, 3269 (2019).
53. Tam, C. C. et al. Charge density waves and Fermi surface reconstruction in the clean overdoped cuprate superconductor $Tl_2Ba_2CuO_{6+\delta}$. *Nat. Commun.* **13**, 570 (2022).
54. Loret, B. et al. Crystal growth and characterization of HgBa2Ca2Cu3O8+δ superconductors with the highest critical temperature at ambient pressure. *Inorg. Chem.* **56**, 9396–9399 (2017).
55. Coffey, T. et al. Measuring radio frequency properties of materials in pulsed magnetic fields with a tunnel diode oscillator. *Rev. Sci. Instrum.* **71**, 4600–4606 (2000).
56. Drigo, L., Durantel, F., Audouard, A. & Ballon, G. Tunnel diode oscillator-based measurement of quantum oscillations amplitude in pulsed high magnetic fields: a quantitative field-dependent study. *Eur. Phys. J. Appl. Phys.* **52**, 10401 (2010).

Acknowledgements

W.A.A. acknowledges the support of the Natural Sciences and Engineering Research Council of Canada (NSERC). This work was made possible by the facilities of the Shared Hierarchical Academic Research Computing Network (www.sharcnet.ca) and the Digital Research Alliance of Canada. D.V., D.C., and C.P. acknowledge support from the EUR grant NanoX n°ANR-17-EURE-0009 and from the ANR grant NEPTUN n°ANR-19-CE30-0019-01. This work was supported by LNCMI-CNRS, members of the European Magnetic Field Laboratory (EMFL).

Author contributions

V.O., S.B., N.B., D.V., and C.P. performed the TDO measurements. I.G., V.O., D.V., and C.P. performed the Hall effect measurements. W.A.A. performed the calculations. A.F. and D.C. grew, annealed the single crystals, and performed SQUID measurements. W.A.A. and C.P. supervised the project and wrote the manuscript with inputs from all the authors.

Competing interests

The authors declare no competing interests.

Additional information

Supplementary information The online version contains supplementary material available at https://doi.org/10.1038/s41535-024-00688-6.

Correspondence and requests for materials should be addressed to W. A. Atkinson or C. Proust.